First-principles calculation of electronic and structural properties of $YBa_2Cu_3O_{6+y}$

Giorgia M. Lopez, Alessio Filippetti, Mauro Mantega, and Vincenzo Fiorentini
CNR-IOM (UOS Cagliari) and Dipartimento di Fisica, Università di Cagliari, Cittadella Universitaria, I-09042 Monserrato (CA), Italy

(Received 3 April 2010; revised manuscript received 6 August 2010; published 16 November 2010)

The normal state of the prototypical high-T_c superconductor $YBa_2Cu_3O_{6+y}$ is described via advanced *ab initio* band-theory techniques suited for strongly correlated materials. We describe the system at generic oxygen doping y between the Mott-insulating limit ($y=0$) and the optimally doped Fermi liquid ($y=1$), exploring the metal-insulating transitions related to the paramagnetic-antiferromagnetic competition in the CuO_2 planes, and to the order-disorder competition in the CuO_y chains. Our study demonstrates the usefulness of *ab initio* calculations based on density-functional theory, when suitably adapted to strongly correlated systems, to describe doped cuprates.

DOI: 10.1103/PhysRevB.82.195122 PACS number(s): 71.15.Mb, 71.30.+h, 71.20.−b, 74.72.−h

I. INTRODUCTION

Doped-cuprate high-T_c superconductors have been known and studied theoretically for over 20 years but it is fair to say that a satisfactory theoretical description of their properties at generic doping is largely unaccomplished. The lion's share of theoretical activity belongs to model Hamiltonians of the Hubbard type, which synthesize the essentials of strong correlation physics into a single-band problem with a few parameters but whose ability to capture realistically the intricacies of the many degree of freedoms at play in these systems remains to be proved. For instance, the phase diagram of $Y_{1-x}Ca_xBa_2Cu_3O_{6+y}$ recently obtained by μRS experiments[1] suggests that single-band approaches may not be adequate at all, as O and Ca doping act quite asymmetrically on the electronic and structural properties.[2]

Realistic *ab initio* electronic-structure calculations are ideal to shed light on such complicated phenomenologies. However, to describe strongly correlated systems combining localized, hybridized, and delocalized electrons, a theory will have to work reliably all the way from a strongly localized insulating limit to free-electronlike metals. This is often not the case: density-functional theory in the local spin-density approximation (LSDA) or generalized-gradient approximation (GGA) fail the treatment of localized electrons due to the local exchange-correlation screening while e.g., Hartree-Fock exaggerates the insulating character and misses the metallic state altogether, due to the lack of correlation energy.

Indeed, first-principles approaches have hardly been applied at all to the prototypical doped cuprate $YBa_2Cu_3O_{6+y}$ away from the optimal doping limit $y=1$. Only one report[3] addressed realistically different doping levels, treating $YBa_2Cu_3O_6$ and structurally ordered phases of $YBa_2Cu_3O_{6.5}$ and $YBa_2Cu_3O_7$. We recently studied[4] low-x $Y_{1-x}Ca_xBa_2Cu_3O_6$, but the treatment of oxygen doping, with its structural complicacies, is completely different and far more challenging. With the partial exception of Ref. 3, a complete study of $YBa_2Cu_3O_{6+y}$ vs doping—from the insulating to the metallic limit and as function of structure and dopant geometry—is still missing.

In this work we therefore apply the pseudoself-interaction correction (pSIC) method[5,6] (Sec. II), to the electronic, structural, and magnetic properties of $YBa_2Cu_3O_{6+y}$ as a function of oxygen doping y. We reported previously on a subset of these results.[7] Here we extend that analysis to the whole oxygen-doping range, giving a detailed account of the mechanisms governing the CuO_y chain formation and its interplay with the other (magnetic-nonmagnetic, structural, metal-insulating) phase transitions. After a methodological summary in Sec. II, we discuss the undoped system in Sec. III, and the doped system in Sec. IV. Summary and outlook are in Sec. V. Throughout the paper, we will refer to $YBa_2Cu_3O_{6+y}$ as YBCO.

II. METHOD

The pSIC method[5,6] eliminates from the LSDA Kohn-Sham single-particle potential the unphysical self-interaction of a given electron with its own charge[8] via a projection scheme akin to that used in pseudopotential theory (hence the "pseudo" prefix). pSIC is free of adjustable parameters and equally applicable to both insulators and metals, and has been used successfully on many materials, notably correlated ones.[5–7,9,10] Its limitation is the lack of variationality, which bars access to structural relaxations. We note that in Ref. 3 doped YBCO was tackled with the full SIC-LSDA scheme.[11,12] Despite the similar original inspiration, pSIC and SIC-LSDA act rather differently and produces quite distinct results. A discussion of the relative merits would take us too far afield, so we refer the interested reader to literature entry points, e.g., Refs. 5 and 6 for the former, and Refs. 3 and 11–13 for the latter.

pSIC calculations are carried out with the homemade code PWSIC using plane wave basis sets and ultrasoft pseudopotentials,[14] with 30 Ry cut-off energy, $6\times6\times6$ special k-point grids for total energy calculations, $12\times12\times12$ special k-point grid and linear tetrahedron interpolation for density of states (DOS), $11\times11\times5$ uniform k-point grids for the Fermi surface (FS). XCRYSDEN (Ref. 15) is used to visualize the calculated FS.

We also use GGA+U method[16] in the Dudarev formulation,[17] as implemented in the VASP (Ref. 18) code. This version of GGA+U only corrects magnetically and/or orbitally polarized states with respect to plain GGA. The

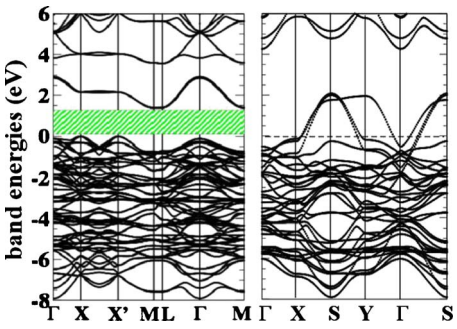

FIG. 1. (Color online) Band energies of undoped, tetragonal G-type AF $YBa_2Cu_3O_6$ (left) and optimally doped, orthorhombic PM $YBa_2Cu_3O_7$ (right) as calculated by pSIC. For $YBCO_6$ the calculation used a $\sqrt{2}\times\sqrt{2}\times 1$ 24-atom cell, and the k-point coordinates in units of $2\pi/a$ and $2\pi/c$ are X=[1/2,0,0], X′ =[0,1/2,0], M=[1/2,1/2,1/2], L=[1/2,1/2,0]. For $YBCO_7$ the cell is $1\times1\times1$ (13 atoms), and X=[1/2,0,0], Y=[0,1/2,0], S =[1/2,1/2,0].

relevant parameter is the difference $U-J$ of on-site repulsion and Coulomb exchange. In all calculations we use a large $U-J=9$ eV which gives a good match with the pSIC-calculated fundamental gap of $YBa_2Cu_3O_6$. In turn, we will see that this value seems to cause disagreement with other observed features of YBCO.[19]

We further use plain GGA for structural optimization in the nonmagnetic phase. pSIC is used for electronic properties and energies at fixed structure.

O doping in several configurations is treated realistically using supercells. At different doping, supercells ranging from 24 atoms [$\sqrt{2}\times\sqrt{2}\times1$, the smallest compatible with antiferromagnetic (AF) ordering] to 96 atoms ($4\times2\times1$) are used. We explored several magnetic phases solving the self-consistent Hamiltonian with appropriate initial magnetization patterns.[20]

III. UNDOPED YBCO

Figure 1 reports the pSIC band structure for the end-point compounds $y=0$ (left panel) and $y=1$ (right panel), respectively. The corresponding atomic structures are sketched in Fig. 2. This is a manifesto of the pSIC ability to accurately describe both the metallic and Mott insulating limits in YBCO. At $y=0$ we find an AF Mott insulator with a gap

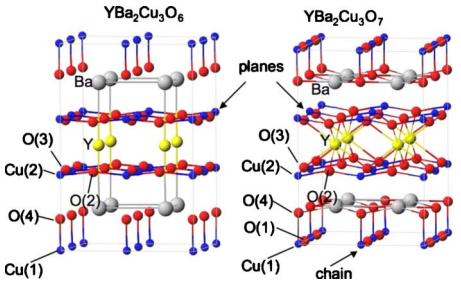

FIG. 2. (Color online) Atomic structures of end-point YBCO compounds: tetragonal $YBa_2Cu_3O_6$ (left) and orthorhombic $YBa_2Cu_3O_7$ (right).

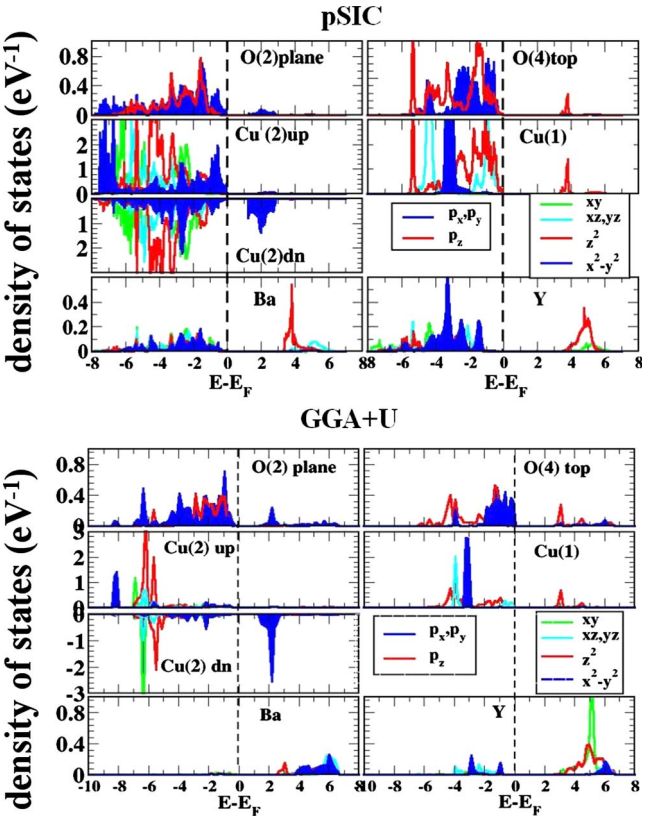

FIG. 3. (Color online) Density of states for undoped insulating AF $YBa_2Cu_3O_6$ projected on d orbitals of Cu, Ba, and Y, and p orbitals of O. Cu(1) and Cu(2) are, respectively, apical unpolarized and planar spin-polarized atoms. Top panels are pSIC; bottom panels are GGA+U. Supercell: $\sqrt{2}\times\sqrt{2}\times2$.

~1.5 eV (thereafter AF will always indicate the G-type antiferromagnetic order observed at low temperature). Due to AF symmetry, each $\sqrt{2}\times\sqrt{2}$ CuO_2 planar unit contributes a twofold-degenerate Cu $d_{x^2-y^2}$/O (p_x,p_y) hybridized band at the valence-band top (VBT) and a hole band of similar orbital character at the conduction-band bottom (CBB). The number of bands contributing to VBT and CBB is further doubled in the picture due to the two CuO_2 planes in the cell. At $y=1$ the bands are those of a metallic Pauli paramagnet (PM) as may be expected for the optimally doped compound. (The small but significant differences between pSIC and GGA/GGA+U for $y=1$ are discussed in Sec. IV E).

The upper panel of Fig. 3 shows the pSIC-calculated orbital-resolved DOS (OR-DOS) for $y=0$. This rendition mirrors consistently the photoemission results. The Mott gap opens between bands with predominant in-plane character. The VBT is a highly hybridized mixture of spin-majority Cu(2)$d_{x^2-y^2}$ states and nonpolarized O(2)p_x [or O(3)p_y] states of the planes while the 1.5-eV-wide hole band is entirely made of minority Cu(2)$d_{x^2-y^2}$ and nonpolarized O(2)p_x [O(3)p_y] states. This classifies undoped YBCO in the intermediate Mott-Hubbard charge-transfer insulator. We also obtain a magnetic moment of 0.45 μ_B per planar Cu, which is in very good agreement with the experimental value.

While the fundamental optical transition connects orbitals within CuO_2 planes, a higher transition (~3.5 eV) involves

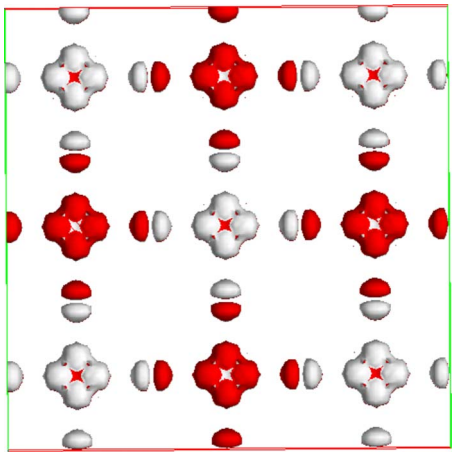

FIG. 4. (Color online) Top view of the pSIC-calculated spin-density isosurface (ρ=0.008 Å^{-3}) of the lowest-energy hole of p-d character in undoped AF YBCO. Red (dark gray) and white (light gray): spin-up and spin-down.

apical O(4)p_z and Cu(1)d_{z^2} states: in the valence these appear ~0.1 eV below the VBT, while they do not contribute at all to the lower hole band. A further flat hole band at ~3.5 eV is instead localized on apical O(4), Cu(1), and Ba d_{z^2}. Even higher in energy is the contribution of Y. Notice also the large difference in valence-band width between planar (~8 eV) and apical states (~5 eV), indicating a higher spatial delocalization (and p-d hybridization) for the former. According to this description, nonplanar contributions to the charge density would be irrelevant in case of rigid-band behavior upon doping; however we will show in the following sections that oxygen doping effects are in no way trivial rigid-band shifts.

Figure 4 reports the density isosurface for the lowest-energy hole calculated in pSIC for the AF phase (this is the band between 1.5 and 3 eV in Fig. 1, left panel). The p and d orbital character and the magnetization pattern of the charge distribution are clearly visualized. Oxygen carries an intra-atomic magnetization integrating to zero by symmetry.

In agreement with observation we obtain the G-type ordering as the most stable. The calculated intraplane J_x (J_y) =−175 meV and interplane J_z=−8.4 meV exchange interactions are in good agreement with experiment. We also considered other types of order. In Fig. 5 we display the band energies for C-type and A-type AF. The former is composed of AF layers aligned ferromagnetically along the c axis, and the latter of ferromagnetic (FM) layers stacked antiferromagnetically along c. C-type ordering has a Mott-type band structure similar to G-type; this is unsurprising because the energy region around the band gap is dominated by in-plane states. The weak interplane FM interaction only removes some degeneracies, notably it splits the two lowest-energy hole bands originating from the CuO_2 planes. On the other hand, the A-type ordering is metalli, because the larger hopping due to in-plane FM alignment of Cu moments (which even spill over on oxygen) causes a large increase in bandwidth (the hole band is more than 3 eV wide) and a band-gap collapse within a small k-space region around Γ.

The pSIC results for the AF electronic properties are used as reference for GGA+U. We find that $U-J$=9 eV, applied

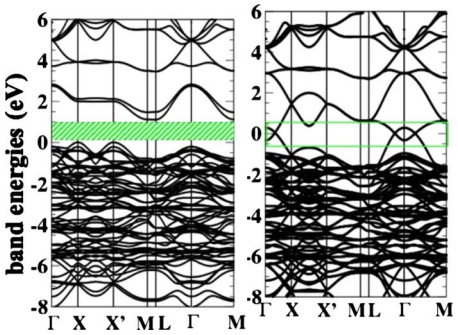

FIG. 5. (Color online) pSIC band energies for C-type (left) and A-type (right) magnetic ordering of undoped YBCO. Fermi energy of C-type aligned with the gap center of A-type. Supercell: $\sqrt{2}\times\sqrt{2}\times 2$. See Fig. 1 for k-point definition.

to both planar and apical Cu, is necessary to open a gap comparable with that of pSIC. Lower values reduce substantially the gap, which closes for $U-J\leq 5$ eV). With $U-J$ fixed at 9 eV, in Fig. 3 we find an overall similarity between GGA+U and pSIC, with one important exception: the VBT is dominated by apical states, with planar states lying ~0.5 eV lower (pSIC places the latter right at VBT). This feature, ultimately deriving from the limited freedom of GGA+U to adjust the fully occupied oxygen and Cu(1) bands, may results in a considerably different doping scenario, and must be kept in mind when analyzing the electronic properties. On the other hand, it has very limited consequences on atomic and structural relaxations (the primary duty of GGA+U hereafter).

In Table I we report structural and internal parameters calculated via energy minimization within GGA for the PM phase, and GGA+U for both PM and the stable AF phase, compared with the experimental data. The agreement with the experiment is overall quite satisfactory, and improves from GGA^{PM} to GGA+U^{PM} and GGA+U^{AF}. The results indicate a good performance of GGA+U for the structural properties, and highlight the somewhat underappreciated virtue of GGA of decently describing structural properties even when the electronic and magnetic properties may be faulty.

IV. OXYGEN DOPING

A. Introduction

A ground-state search at a given oxygen doping requires, in principle, a systematic sampling of possible magnetic states and oxygen configurations. In practice, we choose, among those fitting our computational limits, the ones presumably most pervasive in the phase diagram. At y=1/4 doping, close to the onset of the tetragonal-to-orthorhombic transition, several oxygen configurations have been analyzed. The doping oxygen all aligned to form a single chain, with the superimposed AF ordering, requires a heavyweight 4×2 (96-atom) supercell calculation, at the limit of computing performance for pSIC. At higher doping (y=1/2 and 3/4), 2×2 50-atom cells are sufficient to include chain-aligned (ch) and broken-chain configurations.

Many observations[1,22–26] suggests that static magnetism survives for increasing doping well within the superconduct-

TABLE I. Top section: structural parameters a and c (in angstrom), and Z-axis atomic coordinates (units of c) of tetragonal $YBa_2Cu_3O_6$ calculated by GGA and GGA+U for the PM and AF phases. Experimental values (Ref. 21) shown for comparison. See Fig. 2 for atom labels. Note: $Z_{O(2)}=Z_{O(3)}$; $Z_Y=0.5$ by symmetry. Bottom section: selection of relevant atomic distances (in angstrom) compared to experiment. The buckling parameter δ is the Cu(2)-O(2) distance along Z axis.

	a	c	Z_{Ba}	$Z_{Cu(2)}$	$Z_{O(2)}$	$Z_{O(4)}$
GGA^{PM}	3.91	12.04	0.20	0.36	0.38	0.15
$GGA+U^{PM}$	3.84	12.07	0.19	0.36	0.38	0.15
$GGA+U^{AF}$	3.86	11.90	0.19	0.36	0.38	0.15
Expt.	3.86	11.83	0.19	0.36	0.38	0.15

	Cu(1)-O(4)	Cu(2)-O(4)	Cu(2)-O(2)	δ
GGA^{PM}	1.82	2.57	1.96	0.19
$GGA+U^{PM}$	1.79	2.59	1.93	0.20
$GGA+U^{AF}$	1.79	2.47	1.95	0.24
Expt.	1.81	2.45	1.94	0.22

ing region. In our calculations two phases are obviously included, the PM state supposedly dominant at optimal doping, and the AF phase characterizing the low-doping limit. Once strict AF symmetry is broken, CuO_2 units need not be all equivalent, and a variety of magnetic configurations may be constructed, such as those displaying polarons of various nature, e.g., Zhang-Rice[27] singlets (ZRS), or other more complicated Jahn-Teller double polarons.[28–30] The first-principles description of polaronic states is highly nontrivial and requires a proper treatment of charge localization, which is missed by both LSDA and GGA. Furthermore, polarons appear in a wide variety of patterns (e.g., disorderly scattered through CuO_2 planes or orderly aligned in stripes embedded in AF, PM, or otherwise magnetized regions), further complicated by possible strong couplings between localized holes and atomic displacements. It is thus unsurprising that polarons in cuprates has been so far almost exclusively approached via model Hamiltonians. Early first-principles attempts are limited to two papers.[31,32] Recently we have demonstrated the ability of the pSIC approach to predict and describe polaronic behavior in the context of hole-doped systems such as cation-doped $Y_{1-x}Ca_xBa_2Cu_3O_6$ (Ref. 4) and especially $Ca_{2+x}Y_{2-x}Cu_5O_{10}$ (Ref. 10). While attempt at a generic study of polarons would overcome our computational possibilities, here we apply pSIC calculations to just one highly symmetric ZRS-like configuration with a single polaron within the 2×2 unit cells at $y=1/2$, as a significant prototype of polaronic state.

B. Doping chemistry at $y=1/4$: chain-localized holes

The phenomenology of YBCO is crucially affected by the chemistry and structure of oxygen doping. Unlike Ca doping, understandable as a mere generator of holes "poured" into CuO_2 planes, interstitial oxygen radically change the band structure in a way that cannot be interpreted in terms of Fermi-energy shifts with respect to a rigid-band structure, at any level of approximation. The idea that the goings-on in the CuO_2 planes can be understood in terms of just hole concentration regardless of the doping source is misplaced, and can lead to faulty conclusions. As shown below, the realistic treatment of atomic structure is essential to describe oxygen doping.

At $y=0.25$ one doping oxygen [labeled O(1) hereafter] every four formula units is included between two Cu(1) atoms to form a Cu-O-Cu trimer. As doping increases, the trimers tend to align along a specific direction forming longer and longer chain fragments. A macroscopic evidence of this chain alignment is the tetragonal-orthorhombic transition observed starting at $y\sim0.3-0.4$, concurrently with (and possibly related to) the insulator-metal and superconducting transitions occurring roughly at the same doping. However, this structural transition is not sharp; critical doping depends on sample preparation, which in turn determines formation and length of doped chain fragments.[33] Optical measurements[34,35] indicate that disordered chain fragments start forming at very low doping, giving rise to a finite local conductivity already at $y=0.1-0.2$, although dc conductivity is still absent and the system is regarded as insulator. The rationale[35] is that chain fragments, whose measured average length depends on T and y, are not randomly distributed, but tend to cluster in orthorhombic metallic islands embedded in an oxygen-poor insulating matrix. At increasing doping, the island number and size progressively increases, until they start touching each other at $y\sim0.15$, establishing a continuous pattern of metallic percolation. Finally at $y\sim0.35$ a homogeneous metallic, orthorhombic monodomain is formed.

pSIC calculations strongly support this picture. The key message[7] is that O(1) chain alignment is always *energetically favored over competing arrangements, independently of doping and even of magnetic order in the planes*. In other words, doping oxygen prefer continuous Cu(1)-O(1) chains to isolated Cu(1)-O(1)-Cu(1) trimers. Furthermore, chain alignment gives rise to partially occupied one-dimensional bands lying into the Mott gap. This relates metallicity and chain formation, and establishes a picture for chain formation in full agreement with observations of metallic islands. In this

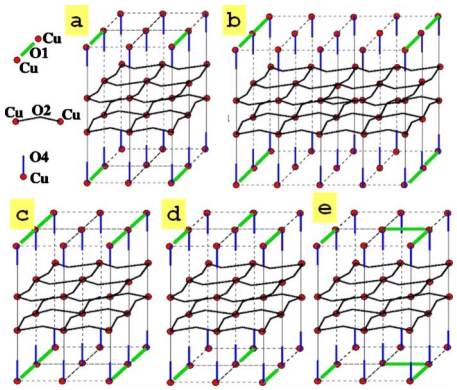

FIG. 6. (Color online) Oxygen-doping configurations studied in this work: (a) $y=0.25$, Cu(1)-O(1)-Cu(1) trimers all in the same direction, one trimer every two steps (broken-chain, planarly orthorhombic); (b) $y=0.25$, chain-aligned configuration, orthorhombic; (c) $y=0.5$, and Cu(1)-O(1)-Cu(1) trimers all chain-aligned; (d) $y=0.5$, broken-chain with all Cu(1)-O(1)-Cu(1) trimers along one direction (orthorhombic); (e) $y=0.5$, and Cu(1)-O(1)-Cu(1) trimers isotropically distributed in the plane (broken-chain tetragonal).

section we analyze in greater detail some results hinted about in Ref. 7.

To explore the energetics at this doping and quantify the tendency toward chain alignment, we consider the configurations schematized in Fig. 6, simulated in 2×2 and 2×4 supercells. The former is sufficient to explore AF and PM phases with unaligned O(1); the latter is needed to compare the relative stability of aligned and unaligned O(1) configurations for the same AF ordering. Unless otherwise specified, all the results shown in this section are obtained by pSIC calculations.

Figure 7 shows the OR-DOS for AF (upper) and PM (lower) phases in the 2×2 supercell for the broken-chain configuration as in sketch (a) of Fig. 6. Left panels refer to in-plane atoms, right panels to apical atoms and doping oxygen. For planar atoms, not much changes with respect to the DOS of the undoped compound (Mott gap $\sim$1.5 eV in the $d_{x^2-y^2}$-p_x,p_y band manifold and Cu magnetic moment $\sim$0.45 μ_B in the AF state). Important changes are instead visible for nonplanar atoms: in the added panels for O(1), a tall peak of p_x character appears, located $\sim$1 eV above the VBT. This spin-degenerate hole is highly localized near O(1) but residually extend up to O(4), mostly p_z, through the adjacent Cu(1), mostly via $d_{x^2-y^2}$ and d_z^2. On the other hand, at first sight the hole seems not to be mixed with in-plane states contributing to the Mott gap. In fact, a closer inspection of the bands, reported in Fig. 8, reveals that the DOS of native and doping hole graze each other around Γ (the coupling mechanism, which transfers to the planes a fraction of 0.05 holes per CuO_2 unit, is described below). Furthermore, the system is clearly insulator. Indeed, it is quite commonsensical[36] that isolated (i.e., not chain-aligned) doping oxygen should not release carriers. Our pSIC calculations are direct quantitative evidence thereof.

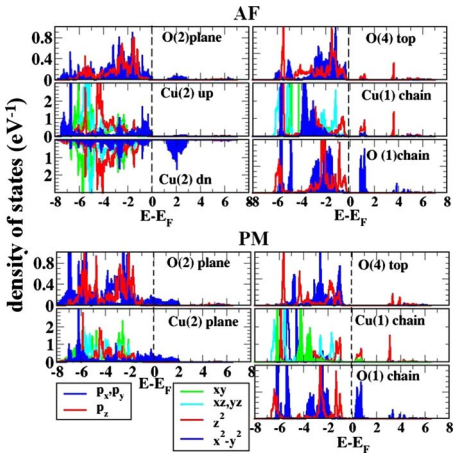

FIG. 7. (Color online) pSIC DOS at $y=1/4$ for the broken-chain configuration of Fig. 6(a), i.e., O(1) forming isolated trimers with the two adjacent Cu(1). Top: AF-ordered planes; bottom: PM planes. In this calculation the Cu(1)-O(1)-Cu(1) segment is oriented along x, thus the doping hole is the O(1)p_x orbital. Supercell: $2\times2\times2$.

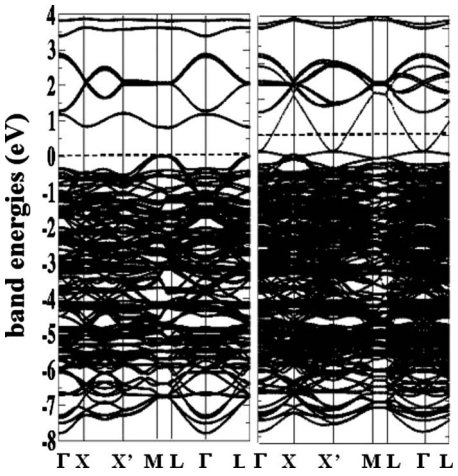

FIG. 8. pSIC band energies at $y=1/4$. Left: broken-chain orthorhombic [panel (a), Fig. 6], $2\times2\times2$ supercell. Right: oxygen-aligned orthorhombic [panel (b) of Fig. 6], $4\times2\times2$ supercell. See Fig. 1 for k-point definition.

The band energies are shown in Fig. 8, left panel: the doping-induced hole is flat throughout the Brillouin zone, its dispersion between the most bonding point X and the least bonding X′ being less than 0.5 eV. [Γ-X and L-X′ are directions parallel and orthogonal to the Cu(1)-O(1)-Cu(1) segment, respectively.] The broader native hole (which now appears downfolded with respect to Fig. 1 due to the 2×2 symmetry) remains well separated in energy all over the zone, except at Γ where the two hole state in question nearly touch.

Consider now the DOS for the PM phase in the lower panel of Fig. 7 (on the left, in-plane atoms; on the right, apical and chain atoms). At variance with the AF phase, there is no gap in the $d_{x^2-y^2}$-p_x,p_y bands, which dominate the region around E_F. The CuO_2 planes are metallic. On the other hand, apical Cu(1), O(4), and O(1) atoms (right panels) behave as in the AF phase, with the O(1)p_x hole still localized $\sim$1 eV above the VBT of the apical-derived states. It appears that planes and chains have substantially decoupled lives at this doping for nonaligned dopants: the chemistry of

planes is insensitive to oxygen inclusion but instead influenced by the magnetization state; vice versa, the DOS of apical atoms barely notices the planar magnetization, but is drastically affected by the O(1) inclusion.

Now we consider, at $y=0.25$, the dopants aligned to form a continuous Cu(1)-O(1) chains. We have used 2×4 supercells allowing AF ordering, as in sketch (b) of Fig. 6. The bands of the AF chain-ordered configuration are in the right panel of Fig. 8. Since at this doping there is one Cu(1)-O(1) chain (parallel to x in our calculation) every four Cu(1) atoms in the y direction, we can assume that chains are decoupled. Unlike the unaligned case, now the doping hole forms a dispersed ($\sim$1.5 eV wide) band. The hole still resides in the chain, and the dispersion is strongly one-dimensional (note the band flatness between L and M). However, the band now overlaps the in-plane native hole band, and even touches the VBT at Γ, so that a coupling is turned on between planes and chains compared with the broken-chain configurations. E_F falls $\sim$0.5 eV above the chain-hole band bottom, in an energy region with no states other than the chain hole itself.

The electronic properties for AF order at $y=0.25$ suggest the following scenario. For nonchain-aligned oxygen configurations CuO_2 planes and CuO_y chains are largely disentangled, since only chains are appreciably influenced by the O(1) inclusions. The flat, spin-degenerate hole states localized in the Cu(1)-O(1) surroundings (bound by the strong electronegativity of oxygen) fall deep-traplike in the Mott gap. This behavior departs from the trivial hole transfer expected, e.g., for Ca doping. Also, it is direct evidence of the widely assumed (but never quantitatively demonstrated) notion, that only a minimal portion of nominal hole charge is actually transferred from doping oxygen to the planes. On the other hand, for oxygen-aligned configurations, O(1) states are still mainly located within the CuO_y region, but since they form widely dispersed bands extending across the Mott gap and largely overlapping in energy with planar states, they establish a coupling channel between chains and planes.

On the other hand, the chemistry of CuO_2 planes is dominated by the magnetization state. Severe changes in the electronic properties of the planes occur when changing magnetic state from AF to PM, i.e., from Mott insulating to metallic Fermi liquid behavior, respectively. More magnetic states will be analyzed at $y=0.5$ doping.

In closing this section, we comment on the presence of aligned but finite Cu(1)-O(1) segments, which are the likely doping patterns at this concentration. We expect the electronic properties of those segments to be intermediate between the chain-aligned and nonchain-aligned configurations just discussed, corresponding respectively to fully formed one-dimensional hole bands and fully localized hole states. Although the modeling of oxygen-aligned segments is computationally prohibitive, total energies strongly suggest oxygen alignment to be favored (see Sec. IV G) with respect to alternative patterns. It follows that longer and longer chains must be expected as doping increases, i.e., more O(1) become available. At low doping, O(1) are scarce and prone to configurational disorder. Yet, according to island clustering scenarios,[35] long chain segments are present even at low doping, and the high-symmetry configurations considered here may be representative of a local (in-island) doping which is much higher than the global (space-averaged) y.

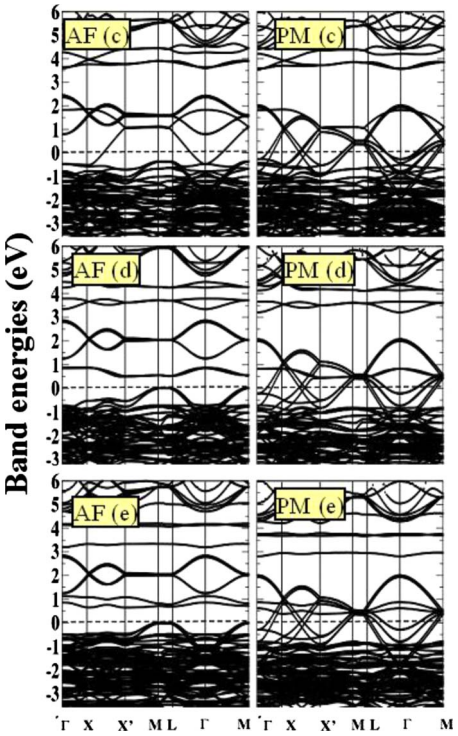

FIG. 9. (Color online) pSIC band energies for AF (left) and PM (right) ordering of $y=1/2$ doped YBCO, for O(1) configurations (c), (d), and (e) of Fig. 6. Supercell: $2\times2\times2$. See Fig. 1 for k-point definition.

C. Electronic properties at $y=1/2$

The chain vs broken-chain competition described in the previous section for $y=1/4$ is weakly dependent on the specific doping, as demonstrated in the following addressing the case $y=1/2$. From a computational viewpoint $y=1/2$ is less cumbersome than $y=1/4$: we can assume that 2×2 unit cells adequately describe the most important oxygen-dopant configurations, at least for the simplest Pauli-PM and AF phases, since configurational entropy has supposedly much less impact, and the system develops a fully orthorhombic [i.e., single-domain O(1)-Cu(1) chain] structure at the expense of the island-textured tetragonal phase. Specifically we consider three configurations (see sketch in Fig. 6): the chain-aligned (c), the broken-chain orthorhombic (d), and the broken-chain tetragonal (e). The corresponding band energies are reported in Fig. 9 for both AF (left panels) and PM (right panels) phases.

We first consider AF ordering, which is easily understood: the planar Mott gap due to the spin polarization is still well visible, despite the overlap with the dopant states. The gap and the shape and dispersion of the VBT and CBB planar bands do not change significantly compared to lower doping (see $y=0$ in Fig. 1 and $y=1/4$ in Fig. 8), another indication of weak chain-plane coupling. As for the doping states, they crucially depend on the O(1) configuration: chain-aligned (c)

TABLE II. Change in orbital occupations upon insertion of an O(1) atom, calculated in pSIC as difference between $y=0$ and $y=1/2$ in $2\times2\times2$ supercells. The + and − signs mean holes and electrons, respectively. "ch" and "bc" refer to the chain-aligned and orthorhombic broken-chain doping configurations [(c) and (d) in Fig. 6], respectively.

	PM ch	AF ch	PM bc	AF bc
O(1)	−0.403	−0.401	−0.364	−0.361
CuO_2 apical	0.373	0.382	0.341	0.348
CuO_2 planar	0.030	0.018	0.022	0.012

bands are one-dimensional, widely dispersed, and span the gap intersecting both the VBT and CBB; overall, they closely resemble those of pattern (b) at $y=1/4$ (Fig. 8). The same goes for the bands of the broken-chain orthogonal pattern (d), similar to that of pattern (a) at lower concentration (Fig. 8). The result for configuration (e), with two contiguous but nonaligned O(1)'s, is intermediate: the corresponding defect states are still localized, but have wider bandwidth than in (d). Notice that in (d) the single flat band is actually a nearly degenerate doublet [as there are two doped Cu(1)-O(1)-Cu(1) trimers in the unit cell, see Fig. 6] and the near degeneracy indicates small coupling between the doped trimers. In (e) this doublet opens up, due to the interaction between the two corner-sharing trimers.

In the PM phase, the bands for the corresponding oxygen configurations (right panels of Fig. 9) are a superposition of planar and chain-derived states. However, a close look easily distinguishes the chain and broken-chain bands. In the former, the bands around E_F are rather dispersed (except along Γ-X and X′-M-L segments, which do not include the chain direction $\hat{y}$). In the latter, flat bands run throughout the zone at about 1 eV above E_F, intersecting the dispersed in-plane bands of the PM phase.

The results discussed so far might then suggest a substantial decoupling of planes and chains, the first only affected by magnetic ordering, the latter by oxygen-doping distribution. However, there are sizable differences in orbital occupations (i.e., integrated OR-DOS) upon doping depending on the magnetic phase and oxygen pattern, along with the plane-chain coupling. A useful proxy in this analysis is the doping-hole redistribution in the various atomic orbitals. Table II reports a synopsis of the most relevant data (also discussed in part in Ref. 7), namely, the hole redistribution between apical and planar atoms, obtained as changes in orbital occupations between $y=0$ and $y=0.5$. Consider first the PM ch phase: due to its strong electronegativity, each O(1) dopant grabs about 0.4 electrons from the system. The corresponding hole charge of $0.37(\simeq92\%)$ and $0.03(\simeq8\%)$ is redistributed to apical and planar atoms, respectively. As expected, most of the hole remains in the region around O(1). For the AF (ch) configuration the numbers are similar but the slightly smaller planar contribution signals a less effective hole transmission to the planes for the AF phase. Looking at the broken-chain case, we notice a sizable decrease in effective doping with respect to chain-aligned cases. Isolated dopants are less effective in stealing electrons from (injecting holes to) the surrounding atoms. The relative efficiency of PM vs AF is similar.

These results suggest interesting considerations on the hole distribution in planes and chains. At low doping, isolated trimers will keep holes anchored on apical regions, hence hardly available for transfer onto the plane and for conductivity (this mirrors the experimental fact that below a doping threshold $y_t\sim0.15$, no in-plane holes are detected by thermoelectric measurements). As doping increases, trimers start clustering and dispersed bands form, spanning the Mott gap and opening up channels of hole injection into the planes. According to experiment,[37] above the hole-injection threshold y_t the normal-state system remains highly resistive at least up to about $y=0.5$ (i.e., well above the superconducting threshold $y_c\sim0.3$); the corresponding planar hole density is $h\sim0.1$, which is also the estimated threshold for spin-polarization extinction.[1,22] This suggests that our results for the doped AF configurations are a more faithful representation of low-doping behavior than the corresponding PM phases. However, according to our band energy results for 1/4 and 1/2 doped AF phases, the CuO_2 planes are insulating (i.e., no metallic holes show up).

How can the in-plane mobile holes be reconciled with the insulating AF phase ? There are at least two straightforward mechanisms to creates holes in the planes. One is dopant clusterization, which, as evidenced here, is effective in reducing the Mott gap, and increases the chain-plane interaction. Aggregation of a larger number of trimers in islands, at the same concentrations considered here, will reduce and eventually close the Mott gap (although proving this directly would require simulations way beyond current capabilities). The second ingredient, not discussed so far, is magnetization disorder introduced by polarons, e.g., ZRS or stripes thereof. In the next section we describe the electronic properties of a ZRS living within our high-symmetry supercell, as an example of how ZRS formation would effectively induce metallic behavior in the planes.

D. Electronic properties of ZRS

Doping-induced polaron formation has been detected in several low-dimensional cuprates, with spontaneous charge localization arising both with or without phonon assistance. ZRS formation in particular was theoretically discussed[27] in the Hubbard model framework. ZRS are believed to compete with other polaronic configurations[29–32,38] within the planes of typical cuprate superconductors. Clearly, a large ZRS population may destroy AF order and dramatically affect the overall magnetic and electronic behavior in the planes.

According to the standard interpretation, a ZRS forms as holes localize on the four oxygen surrounding a certain Cu(2), in order to minimize the strong electrostatic repulsion with the native d hole on Cu(2) itself. Native and doping-induced holes couple to form a two-particle system, with the singlet energetically favored over the triplet, so that the corresponding Cu-O plaquette is spinless. In our calculation the ZRS materializes as a hole spin density (which is, in principle, that of the true interacting-electron system) mainly localized on the surrounding O(2) atoms and spin antipaired to

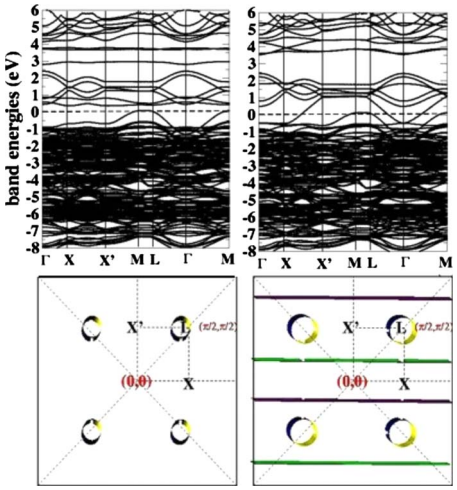

FIG. 10. (Color online) Top panels: pSIC band energies for one ZRS in YBCO at $y=1/2$, in the broken-chain (left) and chain-aligned (right) dopant configuration [panels (e) and (c) in Fig. 6], calculated in the $2\times2\times2$ supercell. Bottom panels: the corresponding FS plotted in the 1×1 Brillouin zone.

the magnetization of the native Cu(2) hole, so that the integrated spin density on the considered plaquette vanishes. Thus we use the term "singlet" somewhat loosely to indicate an assembly of spin-polarized objects whose overall magnetization density vanishes locally within some sensibly defined spatial bounds. This feature is compatible with the experimental observation and represents the counterpart, at the band-theory level, of the two-particle state of the model.[39]

We now describe an isolated ZRS in the 2×2 AF-ordered plane for two doping configurations, i.e., the chain-aligned (c) and the broken-chain tetragonal (e) pattern. In order to obtain stable ZRS solutions, we need to freeze-in a distortion of the CuO_4 plaquette where we intend to induce the ZRS formation. Somewhat arbitrarily, we elect to shift the four O(2)'s toward a Cu(2) by 1% of the Cu-O distance, assigning to each O a starting magnetic moment opposite to that of nearby Cu, and letting the system relax to self-consistency (without ionic displacement, the system converges back to homogeneous AF ordering).

Band energies and FS relative to this ZRS state are shown in Fig. 10. Results for broken-chain (e) and chain-aligned (c) arrangements are shown on left and right panels, respectively. Comparing these band structures with those for AF ordering [left panels (e) and (c) of Fig. 9] we see that now the Fermi energy cuts through the top of the VBT. This is not a mere E_F shift, but a topological change in the plane-derived bands related to hole localization. Indeed, the chemistry of the upper in-plane p-d band cut by E_F is better appreciated perusing the OR-DOS displayed in Fig. 11 for the chain-aligned configuration (c). We have labeled $Cu(2)^*$ and $O(2)^*$ the planar atoms relative to the ZRS-populated plaquette, while O(2) and Cu(2) belong to the AF background. We see that only the former show some hole occupancy at E_F, i.e., at a distance from the ZRS the AF-ordered plane remains insulating even upon hole doping while the condensation of one ZRS per 2×2 planar cell causes fractional hole transfer into the plane. We underline that this is a mobile hole charge, not

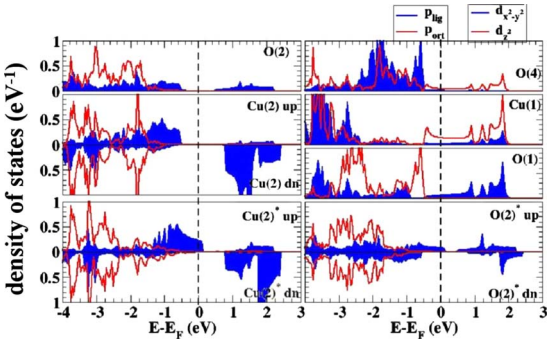

FIG. 11. (Color online) pSIC OR-DOS for one ZRS within AF ordering at $y=1/2$, orthorhombic chain-aligned O(1) [panel (c) of Fig. 6]. Supercell: $2\times2\times2$.

a localized hole charge as described in the previous section, and, in principle, comparable to the hole charge fraction extracted from thermopower measurements.

The spin-compensating nature of the polaron is evident from the OR-DOS. The hybridization between spin-majority $d_{x^2-y^2}$ $Cu(2)^*$ orbital and $O(2)^*$ p ligand (i.e., either p_x or p_y) orbitals causes their magnetization to be always oppositely oriented, i.e., native and polaron-induced holes are spin antipaired. It can be appreciated from the OR-DOS that most of the added hole is still located on apical atoms [Cu(1),O(4)] and doping O(1). This hole charge spreads over a wide energy range (2–3 eV) across E_F, a signature of the chain-related dispersed band. Going back to Fig. 10 (right panels) we can easily distinguish the respective band and FS contributions for planar and chain-apical holes: the former give small pockets centered at nodal points and holelike in character, the latter are one dimensional with a neat parabolic shape around Γ, and electron-like. For the broken-chain tetragonal (e) pattern, the hole trapped on apical atoms remain localized and do not intersect E_F, thus the only FS feature comes from the in-plane hole band. Interestingly, planar and apical contributions to the hole density are not trivially additive: the FS pockets for the broken-chain pattern (left) are visibly smaller than those for the chain-aligned configuration (right), despite the same nominal doping $y=0.5$. Thus, the effective hole concentration in the plane is sensitive to the oxygen-doping ordering in the chains: chainlike order favors stronger interaction between chains and planes, and larger hole charge migration to the planes.

Fermi surfaces and quantum oscillations

Recently, quantum oscillations have been observed[40] in YBCO at $y=0.5$, indicating the existence of small pockets in the FS. At first sight the FS of the ZRS-populated chain-aligned configuration (c) approximates well the pockets inferred from experiment. There are, however, serious discrepancies with experiment, as Shubnikov-de Haas reveals an electronlike, not holelike (as revealed by[41,42] angle-resolved photoemission spectroscopy) FS character, and the measured masses are larger than those calculated. See Ref. 4 and references therein for more discussion, and Ref. 29 for similar proposals involving more complex polarons.

In a different direction, we recall the bands of the AF-A phase (in-plane ferromagnetic) in Fig. 5, and note that closed Fermi pockets of both holelike and electronlike character appear near Γ. This result may have implications for the controversy, as quantum oscillations are observed at low T under strong magnetic field: high fields might locally favor ferromagnetism, and cause the coexistence of nano-sized portions of CuO_2 plane with local FM and AF order, with the attendant appearance of additional pockets such as those in Fig. 5. Of course, this possibility remains to be investigated in detail.

E. Electronic properties at optimal doping

The high-doping regime has been intensively studied in the past by standard first-principles calculations (both LSDA or GGA).[43] At optimal doping, the Mott regime is arguably too far in energy to play a significant role, thus the nonmagnetic Fermi-liquid behavior described by LSDA or GGA is supposedly reliable. The comparison with alternative approaches is still relevant, though. Here we compare pSIC and GGA results for the Pauli PM phase only. GGA+U results are rather close to GGA (Refs. 44 and 45) and are not described here. GGA and pSIC perform similarly at optimal doping but differences appear in the details of the FS.

In Fig. 12 we compare the OR-DOS calculated by GGA and pSIC at $y=1$ [pSIC bands are shown in Fig. 1 (right)]. In both cases the hole is largely redistributed over all atoms (except for Ba and Y states which are barely or not at all touched by E_F). However, the valence band manifold is ~0.5–1 eV wider in pSIC than in GGA, with the hole DOS slightly larger for the former. The main hole peak is at ~2 eV above E_F in pSIC while in GGA the DOS vanishes well below 2 eV. Also, more importantly, in pSIC the orbital character of O(1) and O(4) DOS at E_F is purely p ligand while in GGA the filled manifold of orthogonal p orbitals touches E_F and thus contributes to the FS.

We can better appreciate the difference in the calculated FS (same Figure). Two features are common to both calculations: the typical large cylinders centered at $S=(\pi,\pi)$ derived from CuO_2 planar states, and the one-dimensional sheets (parallel to k_x) related to chainlike O(1)-Cu(1) states. One additional feature is however only present in GGA: the small pockets enclosing (π,π), coming from apical states. The reason for the lack of this feature in pSIC is clear from the bands of YBCO at $y=1$, right panel of Fig. 1: pSIC operates a small downshift with respect to GGA, and the occupied valence band at S is just 0.1 eV below E_F. Apparently, indeed, purely apical (i.e., nonchain-derived) features at FS are not observed by angle-resolved photoemission results,[41] so that the pSIC description seems to be more in line with experiment.

F. Structural parameters vs oxygen doping

In this Section we discuss the structural properties of $YBa_2Cu_3O_{6+y}$ as calculated by GGA and GGA+U. We proceeded first using GGA for the structural optimization of the PM phase in the whole doping concentration range, then applying GGA+U to further refine lattice parameters and

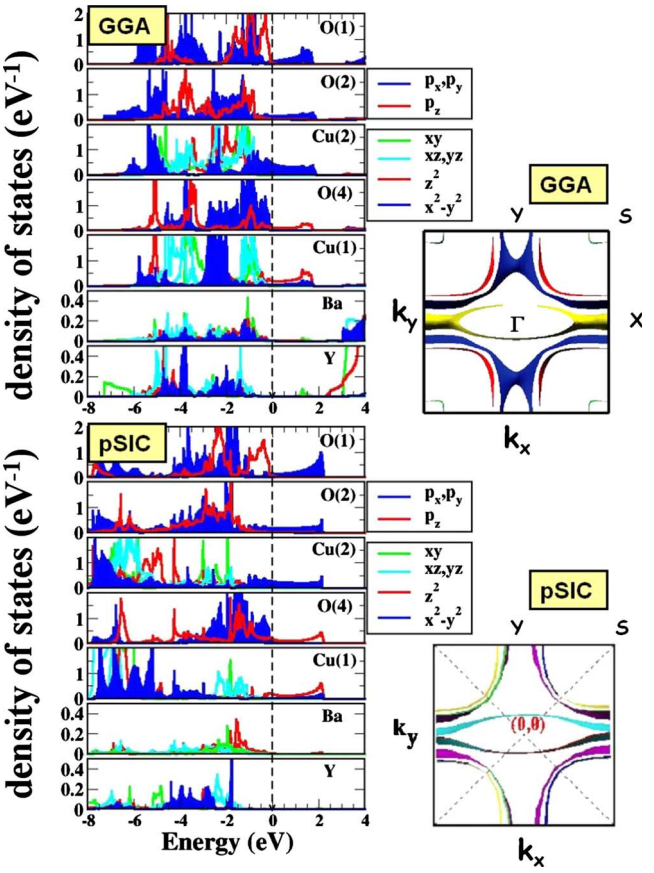

FIG. 12. (Color online) GGA (upper) and pSIC (lower) OR-DOS (left) and FS in the 1×1 zone (right) at $y=1$ for the PM phase. Note the planar orbital character (p_x, etc.) of the hole on O(1), Cu(2), and O(2), and the vertical (p_z, etc.) character on apical Cu(1) and O(4).

atomic positions. Even at low doping, despite the failure in properly treating the Cu(2) spin-polarized hole, GGA is fairly accurate for lattice parameters in comparison with experiment.

Figure 13 summarizes the GGA structural parameters. The structure depends on the dopant configuration: for definiteness we assume the broken-chain orthorhombic configuration [i.e., panel (a) or (d) in Fig. 6] for y up to 0.5, while for higher y we choose the chain-aligned oxygen configuration. We find a systematic volume decrease, and an increase in planar anisotropy as doping increases: a and b start diverging at y around 1/4 (upper panel), and their difference saturates around $y=0.5$. Doping oxygen are aligned along the a axis, i.e., the cell edge parallel to Cu(1)-O(1): indeed, a shrinks with doping. The in-plane structure anisotropy is $2(b-a)/(b+a)\sim2\%$ at $y=1$. Consistently, in the CuO_2 planes the Cu(2)-O(2)-Cu(2) buckling angles (central panel) increase remarkably (up to ~4.5°) at $y=1$. Meanwhile the structure shrinks in the orthogonal direction (c decreases by ~5% from $y=0$ to $y=1$, upper panel in the Figure). This is mainly related to the large decrease in planar-apical distances [Cu(2)-O(4) shrinks by 15%, see lower panel]. The trends described by GGA are largely confirmed by GGA+U (not shown: planar anisotropy 2%, δc 2%, buckling angles increased by 2°). Overall, the GGA (and GGA+U) structure vs

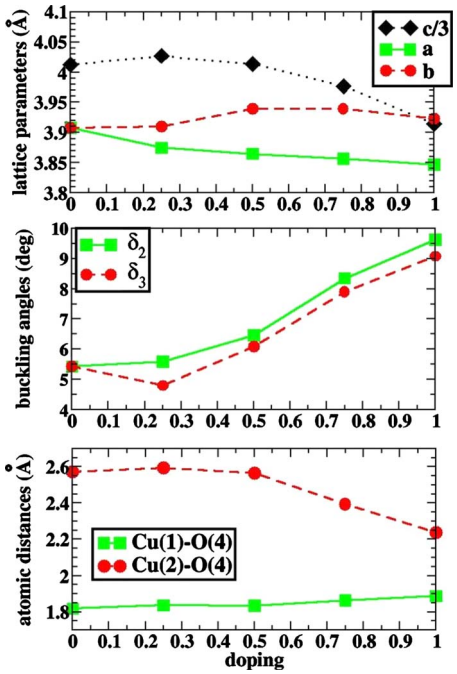

FIG. 13. (Color online) GGA structural parameters vs doping for the PM phase. Upper panel: lattice constants; central panel: in-plane buckling angles; lower panel: apical-atom distances. For consistency the broken-chain oxygen configuration is considered for $y \leq 0.5$; for $y \geq 0.75$ the $2 \times 2 \times 2$ supercell with one filled and one broken chain is used.

doping appears internally consistent, and in decent agreement with experiment (see Table I).

Finally, we comment on the tetragonal-orthorhombic transitions observed at 1/3 doping. According to the prevailing understanding, the transition is associated to oxygen alignment along a specific planar direction. Indeed, our energetics (next Section) confirms that doping oxygen like to align with Cu(1) atoms. However, at low doping the x and y directions are undistinguishable, thus local aggregation of chains proceeds in the form of isotropically distributed domains. At 1/3 doping, chain-aligned domains presumably begin coalescing into large orthorhombic monodomains. According to this picture, below 1/3 doping the observed lattice parameter should be better evaluated as planar average of calculated lattice parameters a, b.

G. Energetics

We now overview the stability of different phases as predicted by pSIC, GGA, and GGA+U in relation to chain formation and oxygen doping level. Table III reports the pSIC total energy results for several oxygen configurations and magnetic states at three values of oxygen concentrations. At zero doping, consistently with experiments the AF phase is stable, and favored by 60 meV over the PM phase. At $y=1/4$, the chain-aligned (b) configuration is favored over the chain unaligned (a), while AF ordering is still preferred to PM ordering. Thus, AF (b) is the overall best. Finally, at $y=1/2$ an overall switch between PM (now the lowest) and AF phases occurs, while chain-aligned configuration (c) is still the most favored oxygen configuration.

TABLE III. Total energies (in electron volt per formula unit) calculated for PM and AF ordering and chain-aligned (c) and unaligned [(d) and (e)] O(1) configurations (see Fig. 6) at vs doping y. Reported values refer to the most stable ordering, except for the GGA+U values at $y=0.5$ referred to PM$^{(c)}$ (which is the stable ordering for pSIC and GGA).

	pSIC	GGA+U	GGA
$y=0$			
AF	0	0	
PM	0.060	0.703	
$y=0.25$			
AF$^{(b)}$	0	0	
PM$^{(b)}$	0.0557	0.727	0
AF$^{(a)}$	0.134	0.123	
PM$^{(a)}$	0.1887	0.827	0.086
PM$^{(a)}$-PM$^{(b)}$	0.133	0.1	0.086
AF$^{(a)}$-AF$^{(b)}$	0.134	0.123	
$y=0.5$			
PM$^{(c)}$	0	0	0
AF$^{(c)}$	0.028	−0.773	
PM$^{(e)}$	0.196	−0.02	0.032
AF$^{(e)}$	0.233	−0.8	
PM$^{(d)}$	0.269		
AF$^{(d)}$	0.309		
AF$^{(e)}$-AF$^{(c)}$	0.205	−0.027	
AF$^{(d)}$-AF$^{(c)}$	0.281		
PM$^{(e)}$-PM$^{(c)}$	0.196	−0.02	0.032
PM$^{(d)}$-PM$^{(c)}$	0.269		

Averaging the AF and PM energies over O(1) configurations and extrapolating linearly as function of y, we obtain that the AF-PM phase transition occurs at about $y=0.4$, which is consistent with the doping threshold expected for the transition between Mott-proximal and metallic regime. We find the chain-aligned configurations to be consistently favored over the unaligned. As a reference, at $y=1/4$ for the AF phase, the energy needed to decouple a single fully aligned oxygen chain [Fig. 6(b)] into two broken chains [Fig. 6(a)] is 1.07 eV (i.e., 0.134 eV/f.u., as reported in the table). For the PM phase this energy is nearly the same (0.133 eV/f.u.) thus indicating that the robust driving force toward oxygen alignment is barely affected by magnetic ordering in the planes.

At $y=1/2$ the energy gain for aligned chains compared to broken chains is still around 1 eV per chain (for consistency all values in the table are per formula unit), with differences depending on the specifics. Configuration (e) with two adjacent corner-sharing trimers, e.g., is more stable than (d) by ~0.07 eV/f.u., indicating a tendency toward oxygen clusterization.

In Table III we also report results obtained by GGA for PM configurations and GGA+U for PM and AF configurations. For GGA, the available data are not sufficient to allow

for a meaningful comparison with pSIC. However, GGA is consistent with pSIC at least in sign, i.e., chain-aligned configurations are favored over broken-chain configurations at any doping. The comparison with GGA+U is more problematic. GGA+U tends to over-reward AF ordering over PM at any doping; at $y=1/2$ the AF stability is actually even larger than at $y=0$, as indicated by the negative sign. As for chain formation energies, at $y=1/4$ there is a close similarity in sign and magnitude between pSIC and GGA+U energies, but oddly enough the accord is lost at $y=1/2$, where GGA +U even favors broken-chain configurations (notice the negative sign for $AF^{(e)}$-$AF^{(c)}$).

This discrepancy may be attributed to the large value of U employed. In this large-U range, the total energy is quite sensitive to U, and easily biased toward magnetism. The chosen value of U is nevertheless necessary to recover the Mott-insulating undoped limit, as discussed in Sec. III. Using a doping-dependent U might fix some of these problems but it is unclear what this dependence should be. More studies will be necessary to assess the detailed performance of GGA +U in this context.

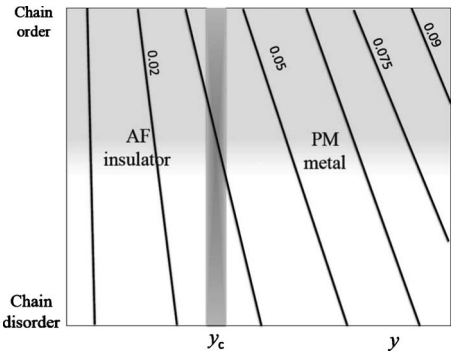

FIG. 14. Schematic phase diagram resulting from pSIC calculations for YBCO. Axes are doping and degree of chain ordering; "AF" and "PM" labels indicate the energetically prevailing magnetic phase; "insulator" and "metal" refer to the existence of a gap in CuO_2-plane-related states; contour lines are the PM-AF difference of chain-to-plane hole transfer (in units of electron charge); the shading along the vertical direction indicates energetic preference upon ordering. Maximal chain-to-plane hole transfer is estimated below 0.2 holes.

V. SUMMARY AND PERSPECTIVES

In this paper we studied $YBa_2Cu_3O_{6+y}$ as a function of oxygen doping. To overcome the difficulties of standard density-functional methods in dealing with Mott-type systems especially across metal-insulator transitions, we employed a self-interaction corrected density-functional method known as pSIC, backed up by GGA and GGA+U calculations. Various doping concentrations, dopant configurations, and magnetic orderings were simulated.

We reported the formation of one-dimensional bands related to chain-aligned O(1)-Cu(1) atoms, leading to in-chain metallization; conversely, planes always remain insulating in the AF phase, and only become metallic in the PM phase. We showed that chain formation energetics always favors ordered chains or portions thereof. Magnetic phase competition as function of doping was considered, and a crossover was found from AF to PM near the expected threshold. We observed that the competition of magnetic vs nonmagnetic and full-chains vs broken-chain are substantially decoupled.

Charge transfer from the chains into planes vs doping was quantified, and found to be always much smaller than expected from simple models: only in the order of a tenth of a hole per Cu is transferred to the planes from doped chains. We gave evidence that chain-to-plane hole transfer is enhanced by two factors: magnetization disorder in the planes and oxygen chain alignment. The fraction of in-plane holes must be a nontrivial function of both magnetic and structural order parameters. Charge transfer efficiency increases from AF to PM and from disordered to ordered chain configuration. The maximal PM-AF hole transfer differential is less than 0.1, and the maximal absolute hole transfer is less than 0.2. Above the $y_c \simeq 0.4$ threshold, quite independently of chain ordering, AF gives way to PM and hence to in-plane metallization (only occurring in the PM phase). Chain ordering energetics hardly depends at all on magnetism and doping in the present zero-temperature picture. Although we did not prove this here, we envisage that the gradual structural transition due to chain ordering, starting near y_c and completing at higher doping, comes about because configurational entropy gradually decreases with y; chain-ordering-induced hole transfer to the plane weakens magnetism and causes in-plane metallization, and is conducive to in-plane hole-mediated superconductivity. We represent synthetically the above statements in a schematic phase diagram in Fig. 14. The axes are doping and degree of chain ordering; the "AF insulator" and "PM metal" labels indicate the favored magnetic phase and the electronic-structure character in the CuO_2 plane (the border between the two around y_c); the shading along the vertical direction indicates energetic gain upon ordering; the contour lines represent the difference in chain-to-plane hole transfer between PM and AF, in units of electron charge.

Future work will have to further push the current boundaries to tackle a general treatment of hole localization in the planes. This requires including localized states such as those giving rise to magnetic polarons (Zhang-Rice singlets, rungs, stripes). Our present showcase analysis, addressed to prove the pSIC ability to describe these exotic objects, was limited to an isolated ZRS in 2×2 symmetry, stabilized by a tentative O(2) breathing displacement. Remarkably, even this "simple" ZRS induces an insulating-metal transition, turning the native, localized Cu(2) holes into conducting two-particle states characterized by a small-pocket Fermi surface. Realistic simulations of polarons are a formidable computational task that will require larger cells plus coupling with local structural distortions. As far as we know, no measurements or calculations of local displacements exist for such doped systems. In a first-principles perspective, the description of

doped cuprate superconductors including polarons is uncharted territory, promising much unexpected physics.

ACKNOWLEDGMENTS

Work supported in part by: the European Union FP7 program under grant Agreements No. 228989 (project "OxIDe") and No. 233553 (project "ATHENA"); Cybersar and CASPUR through supercomputing agreement and grants; Fondazione Banco di Sardegna grant 2010; the Italian Institute of Technology (Project "NEWDFESCM").

[1] S. Sanna, G. Allodi, G. Concas, A. D. Hillier, and R. De Renzi, Phys. Rev. Lett. **93**, 207001 (2004); S. Sanna, F. Coneri, A. Rigoldi, G. Concas, and R. De Renzi, Phys. Rev. B **77**, 224511 (2008); F. Coneri, G. Concas, S. Giblin, A. Rigoldi, S. Sanna, and R. De Renzi, Physica B **404**, 706 (2009); F. Coneri, S. Sanna, K. Zheng, J. Lord, and R. De Renzi, Phys. Rev. B **81**, 104507 (2010).

[2] A feature hardly reconcilable with single-band pictures, indicating the need to account for Cu-O chains and local Ca-induced distortions, is that above the O-doping superconducting threshold $y_t \sim 0.3$, further addition of Ca holes does not affect T_c up to a huge $x \sim 0.1$.

[3] W. M. Temmerman, H. Winter, Z. Szotek, and A. Svane, Phys. Rev. Lett. **86**, 2435 (2001).

[4] A. Filippetti, D. Puggioni, and V. Fiorentini, EPL **88**, 67009 (2009).

[5] A. Filippetti and N. A. Spaldin, Phys. Rev. B **67**, 125109 (2003); **68**, 045111 (2003).

[6] A. Filippetti and V. Fiorentini, Eur. Phys. J. B **71**, 139 (2009).

[7] A. Filippetti, G. M. Lopez, M. Mantega, and V. Fiorentini, Phys. Rev. B **78**, 233103 (2008).

[8] J. P. Perdew and A. Zunger, Phys. Rev. B **23**, 5048 (1981).

[9] A. Filippetti and V. Fiorentini, Phys. Rev. Lett. **95**, 086405 (2005); Phys. Rev. B **74**, 220401(R) (2006); Phys. Rev. Lett. **98**, 196403 (2007).

[10] A. Filippetti and V. Fiorentini, Phys. Rev. B **77**, 235124 (2008).

[11] A. Svane and O. Gunnarsson, Phys. Rev. Lett. **65**, 1148 (1990).

[12] Z. Szotek, W. M. Temmerman, and H. Winter, Physica B **172**, 19 (1991).

[13] M. Stengel and N. A. Spaldin, Phys. Rev. B **77**, 155106 (2008).

[14] D. Vanderbilt, Phys. Rev. B **41**, 7892 (1990).

[15] A. Kokalj, Comput. Mater. Sci. **28**, 155 (2003).

[16] V. I. Anisimov, J. Zaanen, and O. K. Andersen, Phys. Rev. B **44**, 943 (1991).

[17] S. L. Dudarev, G. A. Botton, S. Y. Savrasov, C. J. Humphreys, and A. P. Sutton, Phys. Rev. B **57**, 1505 (1998).

[18] G. Kresse and J. Furthmüller, Comput. Mater. Sci. **6**, 15 (1996); Phys. Rev. B **54**, 11169 (1996); G. Kresse and D. Joubert, *ibid.* **59**, 1758 (1999); The PAW potentials provided with VASP are used. The GGA is by J. P. Perdew, J. A. Chevary, S. H. Vosko, K. A. Jackson, M. R. Pederson, D. J. Singh, and C. Fiolhais, *ibid.* **46**, 6671 (1992).

[19] U comprises effects other than just Hubbard repulsion, hence comparison with experiment is shaky. Yet, our value for underdoped YBCO is not far from the Cu d U of 7–8 eV at optimal doping from Auger data [V. H. S. Moorthy and V. S. Tomar, Supercond. Sci. Technol. **10**, 813 (1997)].

[20] A self-consistent cycle starting with magnetic moments or orbital occupations set according to a magnetization pattern generally converges to a stable state for the same pattern. Heisenberg-model parameters can be extracted from total-energy differences of different magnetic states.

[21] J. S. Swinnea and H. J. Steinfink, J. Mater. Res. **2**, 424 (1987).

[22] Ch. Niedermayer, C. Bernhard, T. Blasius, A. Golnik, A. Moodenbaugh, and J. I. Budnick, Phys. Rev. Lett. **80**, 3843 (1998).

[23] V. Hinkov, S. Pailhes, P. Bourges, Y. Sidis, A. Ivanov, A. Kulakov, C. T. Lin, D. P. Chen, C. Bernhard, and B. Keimer, Nature (London) **430**, 650 (2004); V. Hinkov, P. Bourges, S. Pailhes, Y. Sidis, A. Ivanov, C. D. Frost, T. G. Perring, C. T. Lin, D. P. Chen, and B. Keimer, Nat. Phys. **3**, 780 (2007).

[24] P. Bourges, Y. Sidis, H. F. Fong, L. P. Regnault, J. Bossy, A. Ivanov, and B. Keimer, Science **288**, 1234 (2000).

[25] Y. Sidis, C. Ulrich, P. Bourges, C. Bernhard, C. Niedermayer, L. P. Regnault, N. H. Andersen, and B. Keimer, Phys. Rev. Lett. **86**, 4100 (2001).

[26] B. Fauqué, Y. Sidis, V. Hinkov, S. Pailhès, C. T. Lin, X. Chaud, and P. Bourges, Phys. Rev. Lett. **96**, 197001 (2006).

[27] F. C. Zhang and T. M. Rice, Phys. Rev. B **37**, 3759 (1988).

[28] L. Hozoi and M. Laad, Phys. Rev. Lett. **99**, 256404 (2007).

[29] L. Hozoi, M. S. Laad, and P. Fulde, Phys. Rev. B **78**, 165107 (2008).

[30] H. Keller, A. Bussmann-Holder, and K. A. Müller, Mater. Today **11**, 38 (2008); A. Bussmann-Holder and H. Keller, in *Polarons in Advanced Materials*, Springer Series in Materials Science, edited by A. S. Alexandrov (Springer, Dordrecht, 2007), Vol. 103, p. 599.

[31] V. I. Anisimov, M. A. Korotin, J. Zaanen, and O. K. Andersen, Phys. Rev. Lett. **68**, 345 (1992).

[32] V. I. Anisimov, M. A. Korotin, A. S. Mylnikova, A. V. Kozhevnikov, Dm. M. Korotin, and J. Lorenzana, Phys. Rev. B **70**, 172501 (2004).

[33] *The Physical Properties of High Temperature Superconductors*, edited by C. Ginsberg (World Scientific, Singapore, 1988).

[34] Y.-S. Lee, K. Segawa, Y. Ando, and D. N. Basov, Phys. Rev. Lett. **94**, 137004 (2005).

[35] K. Widder, J. Münzel, M. Göppert, D. Lüerßen, R. Becker, A. Dinger, H. P. Geserich, C. Klingshirn, M. Kläser, G. Müller-Vogt, J. Geerk, and V. M. Burlakov, Physica C **300**, 115 (1998).

[36] G. Uimin, Int. J. Mod. Phys. B **6**, 2291 (1992).

[37] X. F. Sun, K. Segawa, and Y. Ando, Phys. Rev. Lett. **93**, 107001 (2004).

[38] K. Yonemitsu, A. R. Bishop, and J. Lorenzana, Phys. Rev. Lett. **69**, 965 (1992).

[39] The ZRS many-body wavefunction may in fact be built from our single-particle wave functions, e.g., via Wannier-function techniques.

[40] N. Doiron-Leyraud, C. Proust, D. LeBoeuf, J. Levallois, J.-B. Bonnemaison, R. Liang, D. A. Bonn, W. N. Hardy, and L.

Taillefer, Nature (London) **447**, 565 (2007); D. LeBoeuf, N. Doiron-Leyraud, J. Levallois, R. Daou, J.-B. Bonnemaison, N. E. Hussey, L. Balicas, B. J. Ramshaw, R. Liang, D. A. Bonn, W. N. Hardy, S. Adachi, C. Proust, and L. Taillefer, *ibid.* **450**, 533 (2007); C. Jaudet, D. Vignolles, A. Audouard, J. Levallois, D. LeBoeuf, N. Doiron-Leyraud, B. Vignolle, M. Nardone, A. Zitouni, R. Liang, D. A. Bonn, W. N. Hardy, L. Taillefer, and C. Proust, Phys. Rev. Lett. **100**, 187005 (2008).

[41] A. Damascelli, Z. Hussain, and Z.-X. Shen, Rev. Mod. Phys. **75**, 473 (2003).

[42] M. R. Norman, H. Ding, M. Randeria, J. C. Campuzano, T. Yokoya, T. Takeuchi, T. Takahashi, T. Mochiku, K. Kadowaki, P. Guptasarma, and D. G. Hinks, Nature (London) **392**, 157 (1998); M. A. Hossain, J. D. F. Mottershead, D. Fournier, A. Bostwick, J. L. McChesney, E. Rotenberg, R. Liang, W. N. Hardy, G. A. Sawatzky, I. S. Elfimov, D. A. Bonn, and A. Damascelli, Nat. Phys. **4**, 527 (2008).

[43] A minimal selection includes W. Pickett, Rev. Mod. Phys. **61**, 433 (1989); W. E. Pickett, R. E. Cohen, and H. Krakauer, Phys. Rev. B **42**, 8764 (1990); I. S. Elfimov, G. A. Sawatzky, and A. Damascelli, *ibid.* **77**, 060504(R) (2008), and references therein.

[44] D. Puggioni, A. Filippetti, and V. Fiorentini, Phys. Rev. B **79**, 064519 (2009).

[45] In the original formulation (Ref. 16) spin-paired or orbitally unpolarized states are uncorrelated, hence reduced back to their LSDA form. pSIC corrections to LSDA, instead, are maximal at full occupation (Ref. 6), and sizable departures from LSDA should be expected even for spin-degenerate states.